Role and Evolution of FeS₂ Cathode Microstructure in Argyrodite-Based All-Solid-State Lithium-Sulfur Batteries

Matilde Pavan, Konrad Münch, Sebastian L. Benz, Tim Bernges, Anja Henss, Wolfgang G. Zeier, and Jürgen Janek*



Cite This: Chem. Mater. 2025, 37, 3185-3196



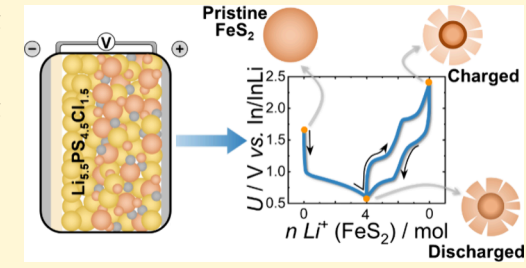
ACCESS I

Metrics & More

Article Recommendations

Supporting Information

ABSTRACT: All-solid-state lithium-sulfur batteries (ASSLSBs) are emerging as a promising alternative for green energy storage, offering high theoretical capacities and energy densities by using inexpensive materials. To date, ASSLSBs commonly suffer from poor cycle life and sluggish reaction kinetics. A promising active material for ASSLSBs is iron disulfide, FeS2, due to its natural abundance, low cost, and high theoretical capacity (894 mAh·g⁻¹). It undergoes a displacement reaction with significant volume changes whose effects can be locally constrained by using small particles. Here, the influence of the positive electrode microstructure on the electrochemical performance of FeS2-based ASSLSBs with Cl-rich argyrodite, Li_{5.5}PS_{4.5}Cl_{1.5}, a mechanically soft sulfide solid



electrolyte with high ionic conductivity, is investigated. Composites with different microstructures were prepared using three different processing methods (i.e., hand grinding, ball mill, and mini mill). Their impact on the electrochemical performance was evaluated, revealing that homogeneously submicro-structured composites achieve higher capacities (up to 4.28 mAh·cm⁻²) and capacity retention (87.2% at the 50th cycle). Furthermore, finely structured composites enhance the in situ formation of active material from the solid electrolyte and increase its accessible reversible capacity. Ex situ analyses (i.e., SEM-EDS and XPS) at different states of charge show that the morphology of FeS2 evolves forming core-shell like submicro-structures.

1. INTRODUCTION

Lithium-ion batteries (LIBs) are currently the most effective electrochemical energy storage technology due to their exceptional energy and power densities, cyclability, and reliability. Typically, LIBs rely on nonaqueous liquid electrolytes (LEs), an intercalated lithium transition metal oxide as cathode active material, and a graphite material as anode active material. This class of cathode active materials (CAMs) includes commercially available materials such as LiCoO₂, $LiNi_{0.8}Co_{0.1}Mn_{0.1}O_2$, and $LiNi_{0.8}Co_{0.15}Al_{0.05}O_2$ that enable theoretical specific capacities of 250-300 mAh·g⁻¹ and volumetric capacities of 1300 mAh·cm⁻³. LIB technology has been vastly investigated and improved in the last decades, and it is now approaching its theoretical limits. Therefore, new technologies need to be developed with higher energy and power densities. Moreover, with increasing energy and power densities demand, LIBs can have safety issues related to flammable LEs, cost and availability issues relying on critical elements like cobalt and nickel.³ Hence, new energy storage technologies must be developed to satisfy the ever-increasing commercial demand and complement LIBs.

A promising technology that allows greater theoretical capacity and specific energy at lower materials' cost is the lithium-sulfur (Li-S) battery. This employs CAMs with a multi-electron storage mechanism that is characteristic of CAMs in which a conversion reaction occurs. One typical

example of conversion-type CAMs is elemental sulfur. Unfortunately, the sulfur conversion reaction involves S₈ and Li₂S as end members of complex redox chains, both being electronic insulators ($\sigma(S_8) \approx 10^{-17} \text{ S} \cdot \text{cm}^{-1}$ and $\sigma(\text{Li}_2\text{S}) \approx$ 10⁻¹³ S⋅cm⁻¹). This, combined with the large volume changes $\Delta_{\rm r}V_{\rm m}$ of its reaction, causes poor cycle life and sluggish reaction kinetics.3-9

Other well-known sulfur-derived conversion-type CAMs are metal sulfides. These are based on a double redox process that involves both the cation and the anion. 10,11 Among these, iron disulfide (FeS₂) is particularly attractive as it is cheap, earthabundant, and non-toxic. It was indeed used as cathode active material at the beginning of the development of ASSLSBs. 12 It exists in nature in two polymorphs, marcasite and pyrite, both containing disulfide S₂²⁻ ions and iron Fe²⁺ ions. ¹³, ¹⁴ Pyrite is the most stable form and has a cubic crystal structure (space group Pa3). Iron disulfide permits partial overcoming of the reaction limitations of sulfur since conductive species (i.e., Fe and FeS) are formed during its (de)lithiation. Its conversion

December 5, 2024 Received: Revised: April 13, 2025 Accepted: April 14, 2025 Published: April 25, 2025





Table 1. Properties of the Reactions of FeS2, S8, and NCM811 with Lithium at 25 °C

	Material		
	FeS ₂	S ₈	NCM811
Cell reaction	$FeS_2 + 4Li \rightarrow Fe + 2Li_2S \text{ (ref 15)}$	$S_8 + 16Li \rightarrow 8Li_2S \text{ (ref 4)}$	$Li_{1.0}Ni_{0.8}Mn_{0.1}Co_{0.1}O_2 \rightarrow xLi + Li_{1.0-x}Ni_{0.8}Mn_{0.1}Co_{0.1}O_2$ (ref 16)
Number of transferred electrons	4 (ref 17, 18)	16 (ref 15)	<1 (ref 2, 16)
Voltage vs. Li ⁺ /Li [V]	1.6	2.1	3.7
$q_{\rm th}$ by volume [mAh·cm ⁻³]	4470 (ref 2, 20)	3461 (ref 2)	~1300 (ref 3)
q_{th} by weight [mAh·g $^{-1}$]	894 (ref 2, 19)	1672 (ref 2)	~200 (ref 16, 20)
Volume expansion [%]	159 (ref 21)	79 (ref 2)	8 (ref 16)
Electronic conductivity [S·cm ⁻¹]	0.05-3.5 (ref 22)	10 ⁻¹⁷ (ref 8)	10 ⁻⁷ -10 ⁻² (ref 20)
Mohs hardness	6.0-6.5 (ref 2, 23)	1.5-2.5 (ref 23)	/

reaction involves 4 electrons in total and a large electrode expansion during initial lithiation:

$$FeS_2 + 4Li^+ + 4e^- \rightarrow Fe + 2Li_2S \tag{1}$$

The main properties of FeS_2 and of its lithiation reaction 1 are listed in Table 1.

Lithium-based all-solid-state batteries (ASSBs) have attracted considerable attention in the last decade as follow-up technology to LIBs. ASSBs may achieve higher theoretical energies and power densities and overcome the limits of LIBs. For example, the absence of flammable nonaqueous LEs may improve general safety and prevent electrode cross-talk. 1,24,25 Various types of solid electrolytes (SEs) have been investigated. Among these, sulfide-based SEs are attractive for their softness and high ionic conductivity.²⁶ Within the class of sulfide SEs, lithium argyrodites (Li_6PS_5X where $X = Cl_1$ Br, or I) receive special attention as they are inexpensive and have high ionic conductivities. Li₆PS₅Cl and Cl-rich argyrodite (Li_{5.5}PS_{4.5}Cl_{1.5}) present remarkable processability and ionic conductivity (2−3 mS·cm⁻¹ and 8−11 mS·cm⁻¹, respectively). Moreover, the large volume changes of sulfide CAMs can be partially compensated by the softness of argyrodites.^{2,16} On the downside, argyrodites have limited thermodynamic stability (e.g., $\approx 1.7-2.0 \text{ V vs. Li}^+/\text{Li for Li}_6\text{PS}_5\text{Cl}$). Nevertheless, the experimental stability window (SW) of argyrodites is broader than that thermodynamically predicted (e.g., SW(Li₆PS₅Cl) \approx 0.6-2.5 V vs. Li⁺/Li), due to kinetic limitation of the degradation reactions, and it is influenced by material choice, microstructure, and current density. It has been previously demonstrated that argyrodites can work as active material precursors within the potential range 0.0-3.6 V vs. Li⁺/Li by mixing them with carbon. During cycling, the SE in contact with carbon is converted in situ into active material by both phosphorus and sulfur redox reactions.3,14,15 It has been recently shown that this can occur when cycling sulfide CAMs within their voltage stability range (e.g., SW(FeS₂) $\approx 1.0-3.1 \text{ V}$ vs. Li^{+}/Li). $^{27-29}$

FeS₂-based ASSBs, designed for use in electric vehicles, have been reported to have a lower environmental impact, offer higher specific capacity, and have similar cumulative energy demand (CED) and global warming potential (GWP100) compared to LIBs.³⁰ Still, several challenges, including large volume variations and related chemomechanical degradation, remain to be overcome.³¹ A comprehensive understanding of the role of the microstructure of the positive electrode, typically called cathode composite, may help to find solutions for these problems. Indeed, it is known that the positive electrode microstructure can have a significant impact on the

cell performance.^{32–40} Previous studies demonstrated how small particles of active material led to higher capacities and longer capacity retentions.³⁵ Such findings can be rationalized by the high contact area that facilitates the conversion reaction by shortening the diffusion pathways, thus increasing the active material utilization. Furthermore, the large volume changes can be more easily mitigated since they take place homogeneously in the composite.^{35,36} A recent report from Whang *et al.* noted the need for systematic studies on the evolution of the electrochemically formed positive electrode microstructures in ASSLSBs.¹¹ It also highlighted the importance of porosity which can potentially mitigate the large volume changes related to transition metal sulfide lithiation reactions.

Most reports about ASSLSBs based on FeS2 focus on the active material synthesis without investigating the positive electrode microstructure and the CAM contact area with the other components within the composite. Hence, in this work, we synthesized composites with different microstructures by using various easily accessible processing methods, i.e., hand grinding and milling in a mini mill and a ball mill. The different composites were characterized by X-ray Diffraction (XRD), Scanning Electron Microscopy coupled with Energy Dispersive X-ray Spectroscopy (SEM-EDS), and X-ray Photoemission Spectroscopy (XPS), and were electrochemically tested. The different microstructures were then compared to assess their influence on the electrochemical performance of the positive electrodes in half cells. We observed that higher capacities and long-term cycling performances were achieved with more homogeneous and submicro-structured composites. Moreover, the microstructure affected the electrochemical activity of the SE, since it influences its contact surface with carbon additives. The evolution of morphology during cycling and the variation of the chemical composition were investigated by post mortem SEM-EDS and XPS analyses.

2. RESULTS AND DISCUSSION

2.1. Microstructural Characterization of Positive Electrode Composites. The positive electrode microstructure plays a key role in the electrochemical performance of ASSBs. Both the size of domains and the interface area of contact between the different components in the composites (*i.e.*, CAM, SE, and conductive additive) influence ion and electron transport. It is therefore crucial to tune the positive electrode morphology. This can be achieved with two main approaches: fine-tuning the morphology of the pristine components or adjusting the positive electrode processing. The first approach is widely used in scientific literature since it permits regulating the CAM morphology, however, it often

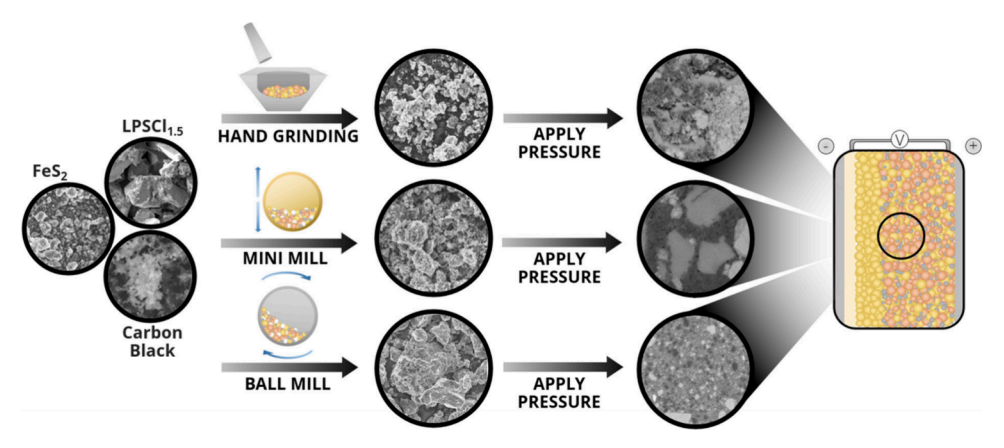


Figure 1. Schematic workflow to investigate the impact of the different positive electrode composite morphologies. The same pristine components (FeS₂, Li_{5,5}PS_{4,5}Cl_{1,5}, and carbon black) were employed and mixed with three different techniques (hand grinding, mini mill, and ball mill). The powder mixtures were then used to build cells by pressing them into pellets (In/InLi | SE | composite). The produced cells were then characterized electrochemically.

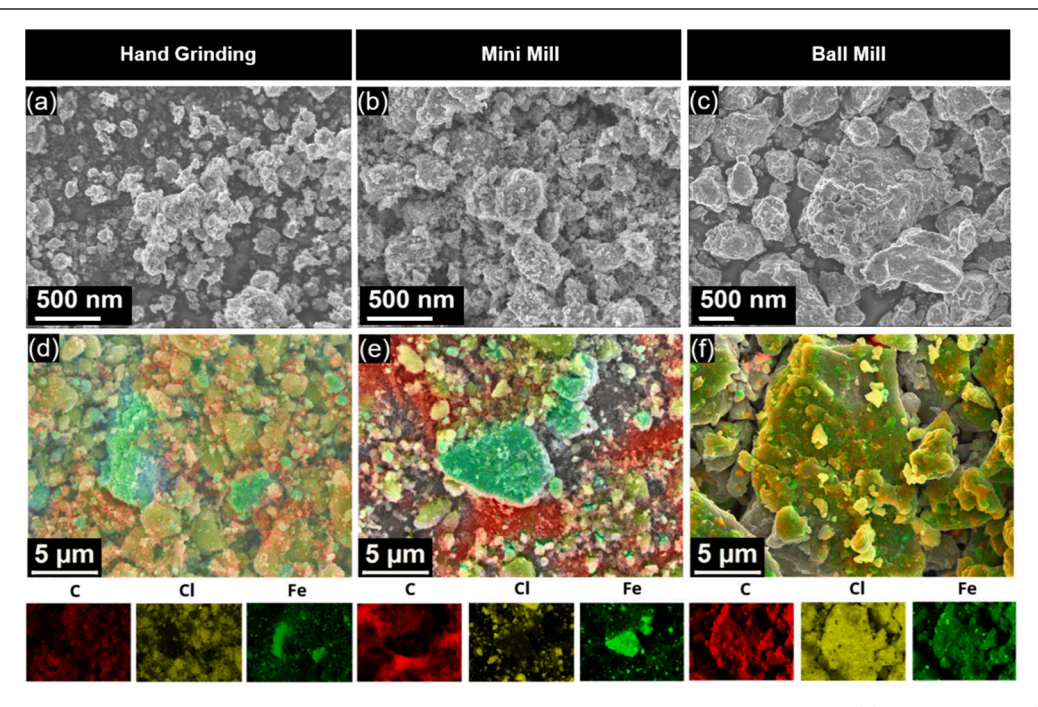


Figure 2. SEM images collected with an SE-InLens detector of the positive electrode composites mixed with (a) hand grinding, (b) mini mill, and (c) ball mill. EDS images showing the elemental map of the positive electrode composites mixed with (d) hand grinding, (e) mini mill, and (f) ball mill. Separate iron (Fe), chlorine (Cl), and carbon (C) maps are shown below with green, yellow, and red signals, respectively. The distribution of carbon indicates the conductive additive, Cl displays the Cl-rich argyrodite, and Fe corresponds to FeS₂.

includes laborious procedures that are hard to scale up. 35,38,41,42 Tuning the positive electrode processing is a more technical top-down approach but it is simpler and cheaper. Moreover, this step is always necessary as last step and it can alter the properties of the pristine components, depending on their mechanical properties. Softer materials with lower Mohs hardness are more prone to deformation during processing compared to harder materials with higher Mohs hardness. We therefore decided to focus on the impact of positive electrode composite processing, which is often neglected. To investigate it, three different mechanical approaches were tested: hand grinding, frequency milling in a mini mill (Fritsch Pulverisette 23), and rotatory milling in a ball mill (Fritsch Pulverisette 7). These techniques were selected because they are widely used on the typical laboratory scale.⁴³ The processes are illustrated schematically in Figure 1,

together with the following workflow for their electrochemical testing.

Prior to mixing the various components for composite preparation, commercial FeS_2 was ball milled to reduce its particle size and make it more suitable for this study. The asreceived material had a particle size of a 325 mesh (\sim 44 μ m). After the ball milling process, particle size reduction was confirmed through SEM images (Supporting Information, Figure S1) and particle size distribution analysis (Supporting Information, Figure S2). Additionally, this processing resulted in a decrease in material crystallinity which is related to the reduced particle size (Supporting Information Figure S3). To evaluate solely the effects of the mixing methods, the same pristine components were employed in all cases. Both, the processed FeS_2 (CAM) and $Li_{5.5}PS_{4.5}Cl_{1.5}$ (LPSCl_{1.5} or SE) were used in the form of micrometer-sized particles: D50 =

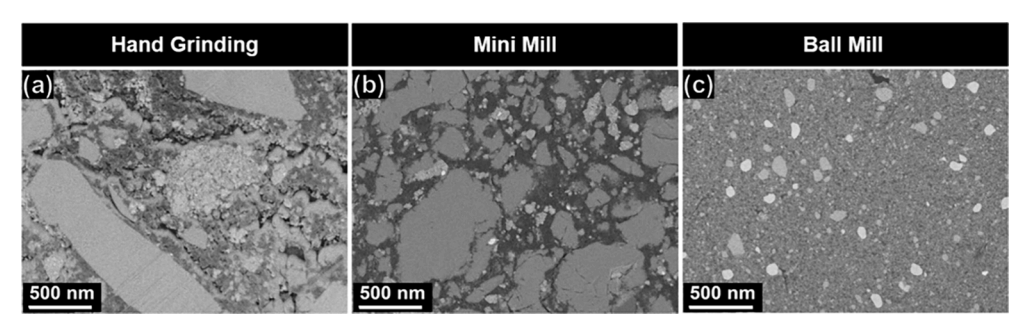


Figure 3. SEM images collected with an EBS detector of the positive electrode composites pressed at 380 MPa. These were mixed with (a) hand grinding, (b) mini mill, and (c) ball mill. The EBS detector allows differentiating between elements with largely different masses; light elements appear with darker gray tones and heavier elements appear with brighter tones. Thus, the black/dark gray parts represent carbon black, the medium gray regions represent LPSCl_{1.5}, and the light gray particles represent FeS₂.

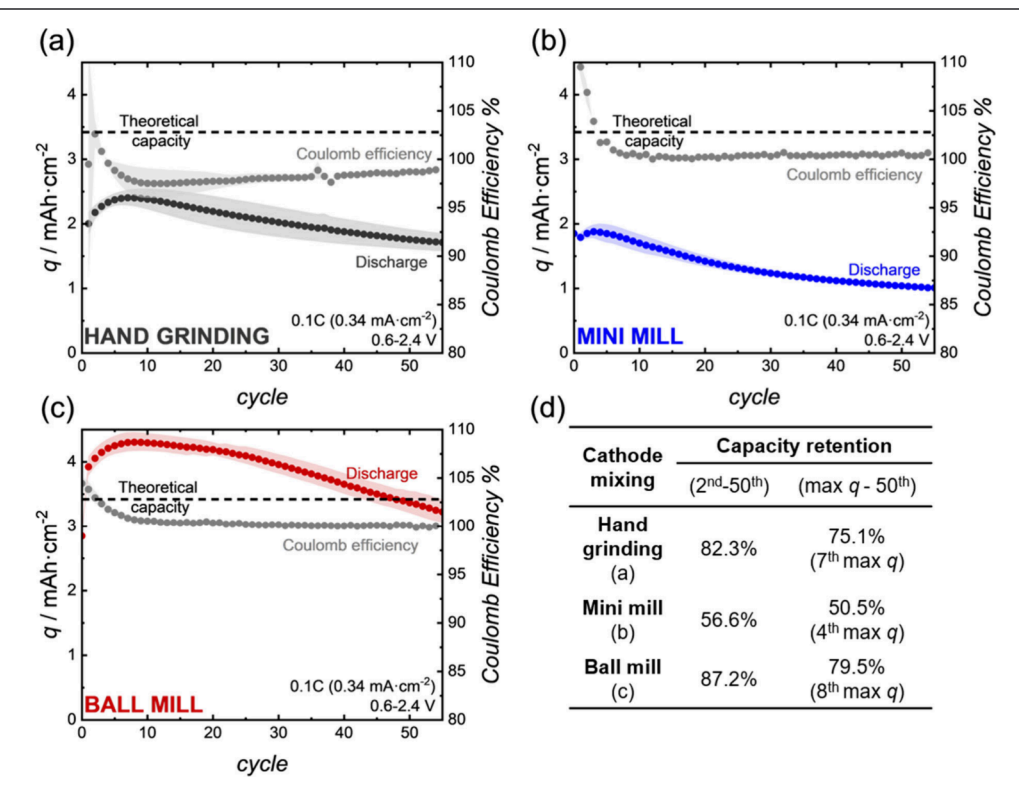


Figure 4. Long-term cycling stability and coulomb efficiency of cells $In/InLi \mid LPSCl_{1.5} \mid FeS_2/LPSCl_{1.5}/carbon$ black. All cells were cycled at 25 °C at 0.1 C (0.34 mA·cm⁻²), and the areal FeS_2 loading was 3.8 mg·cm⁻². The areal capacities reported here are normalized to the electrode area. The positive electrode composites were prepared with (a) hand grinding, (b) mini mill, and (c) ball mill. (d) Table reporting the capacity retentions calculated based on the second cycle or on the maximum capacity measured.

3.73 and 17.35 μ m, respectively, measured with a particle size analyzer. The carbon black (electron-conductive additive) was used in the form of submicro-particles (D50 = 310 nm) with a narrow size distribution (Supporting Information Figures S4—S5).

After mixing, SEM revealed that irregular particles with broad size distributions are obtained with all methods. Hand grinding (Figure 2a) and milling in a mini mill (Figure 2b) formed microsized particles, while ball milling (Figure 2c) produced considerably larger microparticles. In the first two cases, the particles obtained after mixing were significantly smaller than those of the pristine SE and active material, whose particle sizes were measured with a particle size analyzer. The elemental distribution maps, collected with EDS, were used to qualitatively evaluate the mixing quality and the area of contact between the components. The elemental distribution maps

were also employed to detect and differentiate the materials present in the positive electrode composites. Specifically, the signal of iron was used for the active material, FeS2, chlorine for the argyrodite, LPSCl_{1.5}, and carbon for the carbon black. Hand grinding and mini milling, especially the latter, lead to several FeS₂ microparticles being present in the composite. Furthermore, the single particles of each component could still be distinguished. For the ball milled composite, the microparticles were homogeneous agglomerates of all components, within which only submicrometer-sized FeS₂ particles could be distinguished. The crystallinity of the individual components after mixing was assessed using X-ray diffraction patterns reported in Supporting Information Figure S6. Across all mixing methods, FeS2 showed a decrease in crystallinity, suggesting partial amorphization during the mixing processes. In the case of the ball milled composite, the argyrodite also

underwent a significant loss of crystallinity. This phenomenon has already been reported and has recently been systematically studied in the work of Maus $et\ al.$ The latter demonstrated a reduced structural coherence and an increased disorder in $\text{Li}_{5.5}\text{PS}_{4.5}\text{Cl}_{1.5}$ during composite processing, leading to a decrease in its ionic conductivity.

To understand the effect of processing on the microstructure that is formed after densification of the positive electrode composite, SEM images of pelletized composites were investigated (Figure 3). The hand ground and the mini milled composites showed similar microstructures. Figure 3a,b shows well-interconnected frameworks of carbon (black/dark gray particles) linking the argyrodite (gray particles) and the iron disulfide (light gray particles). For the ball milled composite, Figure 3c, no SE particles were observed, LPSCl_{1.5} appeared as a homogeneous matrix in which the other components were finely enclosed. The composite was thus uniform and with micro sized domains of FeS₂ and carbon black. The latter were smaller than those of FeS_2 due to the greater hardness of FeS_2 compared to the inherently soft nature of carbon black, as well as the larger particle size of FeS₂ before mixing. The FeS₂ submicro-particles observed via SEM images, in the ball milled composite suggest an increased CAM surface area which can qualitatively explain an increased contact area, among the positive electrode components, due to the smaller particle size. Therefore, these may be better contacted electrochemically.

2.2. Electrochemical Performance of All-Solid-State **Battery Cells.** The prepared composites were used as positive electrodes in ASSB cells. The long-term cycling performances for the hand ground, mini milled, and ball milled composites are shown in Figure 4a-c, normalized to the electrode area, and in Supporting Information Figure S7a-c, normalized to the FeS₂ mass. The retention improved with more homogeneous and finely dispersed CAM (ball milled composite, Figure 4c), which probably aided in distributing the mechanical stress within the positive electrode. The capacity obtained by ball milling (maximum of 4.28 mAh·cm⁻²) was indeed significantly higher than by hand grinding, Figure 4a, and mini milling, Figure 4b (maxima of 2.44 and 1.94 mAh·cm⁻², respectively). These values can be justified by the larger FeS₂ particles observed for the hand ground and mini milled composites powders, Figure 2d,e and Figure 3a,b. The better performance of the composite prepared by hand grinding compared with that prepared by mini milling can be ascribed to several possible factors. Among these, one of the most relevant is the larger contact between the different components which was observed in the SEM images (Figure 3a,b). This may improve the overall electrochemical performance by enhancing the active material utilization. As in this long-term cycling data, ASSLSBs capacity as a function of the cycle number often shows a maximum. This behavior is typical of sulfide-based CAMs that require some cycles to be completely electrochemically activated. This activation results from kinetic factors, microstructural rearrangements during cycling, and chemical activation of the solid electrolyte. The cycle at which the maximum capacity is reached depends on the properties of the composite (i.e., morphology and composition). The longterm cycling performance is typically quantified in terms of the relative capacity retention between the second and n^{th} cycles of interest. For ASSLSBs it is sometimes reported between the cycle with the maximum capacity (max q) and the nth cycle. To facilitate comparisons, Figure 4d reports the capacity retentions both to the second cycle and to the max q. The

positive electrode composition was kept constant, thus, the position of the maximum was similar, and the capacity retentions reported to the second or max q were comparable. The capacities of all composites were still increasing after the second cycle because of the activation process, so all capacity retentions were larger when referred to it.

The theoretical areal capacity of these cells, considering FeS₂ as a CAM, was 3.42 mAh·cm⁻². The latter is indicated as a black dashed line in Figure 4a-c. As depicted in Figure 4c, the accessible capacity with mixing in a ball mill was larger than theoretically expected on the basis of FeS₂ only. To understand the origin of the additional capacity measured in the ball milled composite, differential capacity plots are studied. Peaks in these plots correspond to electrochemical reactions occurring during cycling, providing insight into the underlying chemistry of the system. In all the differential capacity (dq/dU) plots (Supporting Information Figure S8) the discharge peaks at 0.8 and 1.4 V represent the opposite redox processes at 1.2 and 1.85 V, respectively, observed during charging. However, in the dq/dU plot of the ball milled composite (Supporting Information, Figure S8c), an additional peak at 1.55 V (discharge) and a shoulder at 1.9 V (charge) were present compared to those of the hand ground and the mini milled composites. This indicates the occurrence of a non-negligible reversible secondary process taking place within the more finely dispersed composite. Moreover, the conversion efficiency proved that the rate-determining step (RDS) took place during charging (Supporting Information Figure S9) which is in agreement with previous reports.^{37,46}

We ascribe the superior electrochemical performances of the ball milled positive electrode to the submicro-domains of FeS₂ homogeneously distributed in it (Figure 3c). Apparently, the submicro-sized conversion CAM helps to evenly distribute the large volume variations during cycling, increasing the area of contact and shortening the Li⁺ diffusion paths within FeS₂, thus enhancing the accessible capacity. The surrounding soft electrolyte aided in locally compensating the volume changes and ensuring ionic conduction ($\sigma_{\text{ion,BM}} = 0.10 \text{ mS} \cdot \text{cm}^{-1}$) through the whole composite (Figure 3). Inversely, the other composites presented micrometer-sized domains, lower ionic conductivities, and corresponding capacities ($\sigma_{\text{ion,HG}}$ = 0.05 mS· cm⁻¹ and $\sigma_{\text{ion,MM}}$ = 0.04 mS·cm⁻¹). The large SE particles (medium gray particles) visible in the SEM images were surrounded by well-connected carbon domains (black particles), which resulted in higher electronic partial conductivity compared to the ball milled composite ($\sigma_{\rm el.BM}$ = 10.30 mS·cm⁻¹). All partial conductivities are reported in Supporting Information Figures S10, S11, S12, and S13, and their measurements are described in more detail in Note S1. From these results, we conclude that the domain size of the components in the composite has a larger impact on the electrochemical performances, rather than the crystallinity of the solid electrolyte or the presence of pores. 11,41

2.3. Solid Electrolyte Contribution. It is known that argyrodites can be electrochemically decomposed in contact with carbon at sufficiently high and low potential and then form active material *in situ* which can be cycled reversibly.²⁷ The solid electrolyte involved in this process must be in contact with carbon to be activated; thus, the extent of decomposition depends on the positive electrode microstructure and should be greater within finely structured composites. To evaluate the contribution of the solid electrolyte, composites without FeS₂ were prepared with the

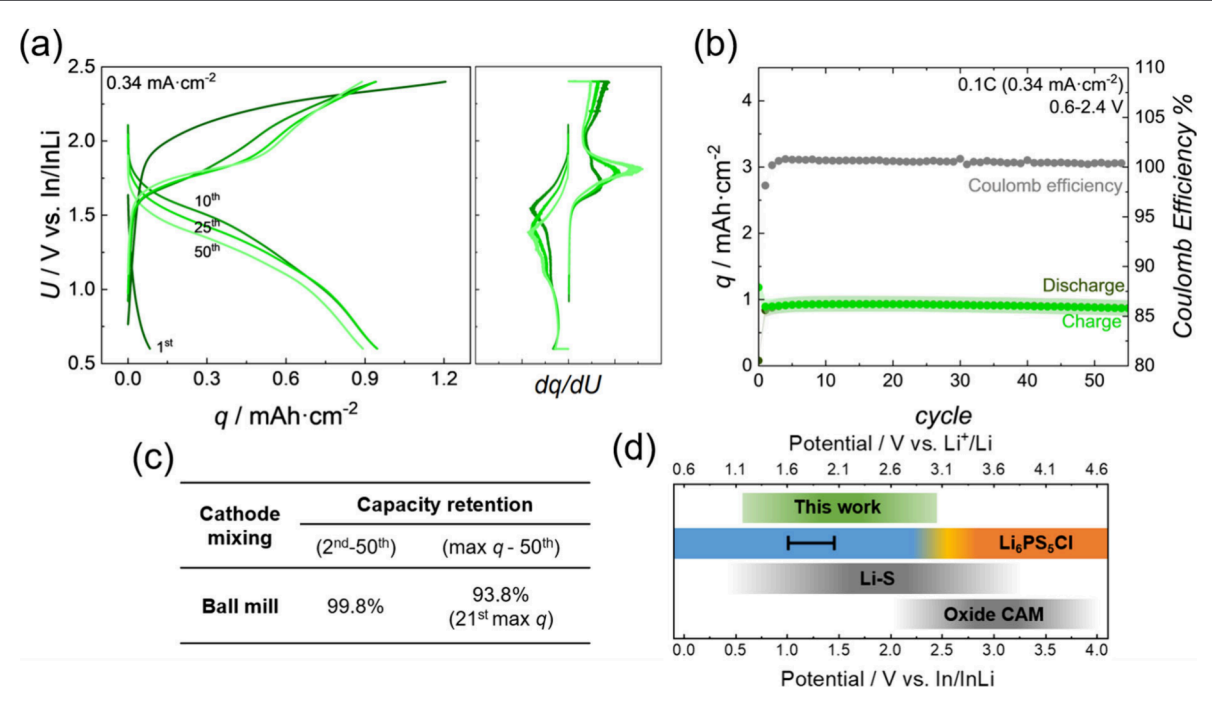


Figure 5. Electrochemical performance of a cell In/InLi | LPSCl_{1.5} | LPSCl_{1.5}/carbon black. The positive electrode composite was prepared with ball milling, and the cell was cycled at 25 °C at 0.34 mA·cm⁻². (a) Charge and discharge voltage with dq/dU plot; the peak at ca. 1.55 V during discharge is due to the sulfur lithiation while the peak around 1.9 V during charge is due to Li₂S delithiation. (b) Long-term cycling stabilities and coulomb efficiency. (c) Table reporting the capacity retentions calculated based on the second cycle or on the cycle with the maximum capacity measured (max q). (d) Overview adapted from Dewald *et al.*; ²⁸ this scheme compares the voltage range of this work, of LPSCl kinetic (blue) and thermodynamic (black line) stabilities. It also shows the typical cycling windows for Li–S and oxide CAM-based cells. Reproduced from ref 28. Copyright 2019 American Chemical Society.

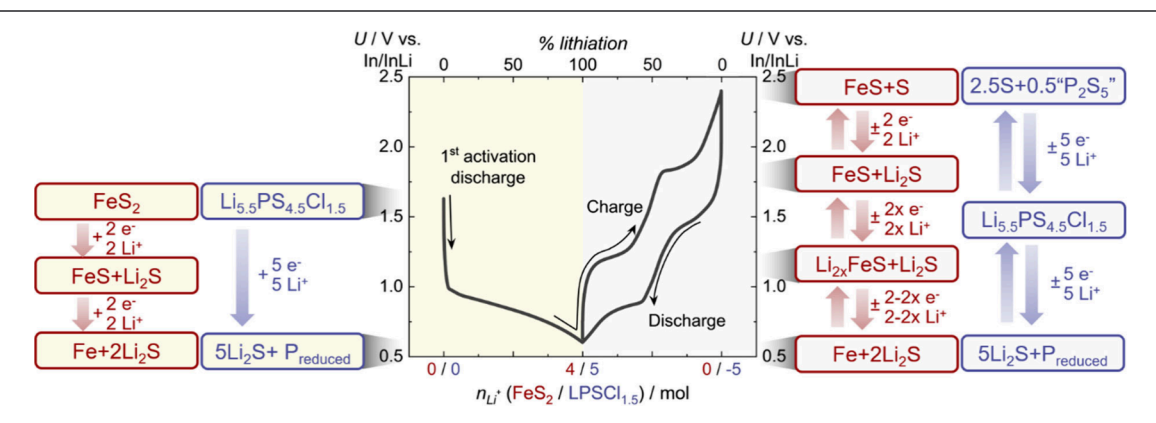


Figure 6. FeS₂ (red) and LPSCl_{1.5} (blue) conversion reaction mechanisms are reported here as a function of the cell voltage. 27,37 The left part of the graph (yellow) shows the first activation discharge, and the right part of the scheme (light gray) shows the following charge and discharge steps. The reaction products and intermediates, the exchanged electrons, and lithium ions are shown in colored frames at the sides. The product reported in quotation marks (i.e., P_2S_5) is unlikely to be present in the electrode due to entropy loss. The identification of which polysulfides are formed is not trivial; therefore, we here suggest " P_2S_5 " formally as a product. Modifying the reaction scheme of Wang *et al.*, we note the formation of $P_{reduced}$ instead of $P_{reduced}$

methods described above. The crystallinity of the solid electrolyte in the positive electrodes was assessed by an X-ray diffraction analysis. The reflections associated with the argyrodite broadened following the mixing process in all composites, regardless of the presence of FeS₂ (Supporting Information Figure S14). The impact of the processing method was thus the same, suggesting the formation of analogue microstructures. The electrochemical test revealed that almost no capacity is released by the hand ground and the mini milled composite, while the ball milled composite has a high reversible capacity of almost 1 mAh·cm⁻² (Figure 5). This

result is supported by the recent work of Qian *et al.*²⁹ The differential capacity plot, in Figure 5a, shows the same signals as those previously seen in only the ball milled positive electrode with FeS₂ (Supporting Information Figure S8c). We attribute these signals to the argyrodite electrochemical activity, specifically to its sulfur and phosphorus redox. The occurrence of this *in situ* activated catholyte can be explained by the finely dispersed carbon black within the solid electrolyte matrix, which provided an increased contact area between the two components. Besides, the potential range (Figure 5d) was within the previously reported kinetic stability range of the

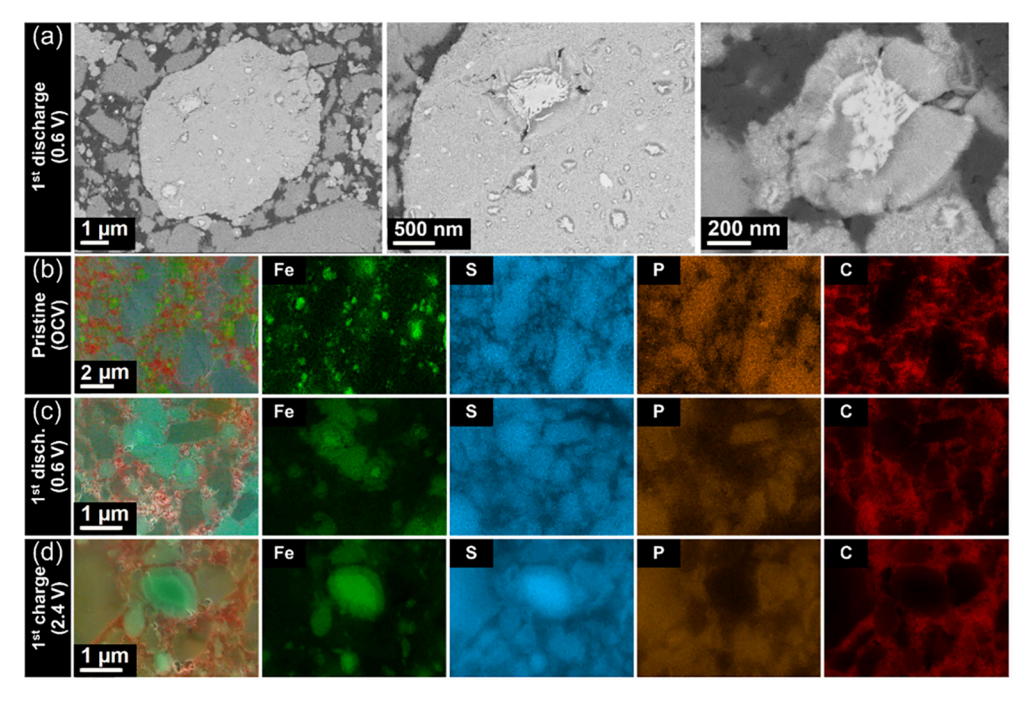


Figure 7. (a) SEM images, at different magnifications, collected with an EBS detector of positive electrode composites prepared in a mini mill after the first discharge. EDS mapping images of the mini milled composites at different states of charge: (b) pristine at the OCV, (c) discharged at 0.6 V, and (d) charged at 2.4 V. Iron (Fe), sulfur (S), phosphorus (P), and carbon (C) separate maps are shown on the right with green, blue, orange, and red signals, respectively.

catholyte. We then evaluated the deconvoluted contributions to the overall capacity coming from the SE and the CAM. According to the calculations reported in Supporting Information Note S2, the maximum contribution of FeS₂ in the ball milled composite (879 mAh·g⁻¹) was almost equal to its theoretical capacity. While for the SE, its contribution to the capacity was more than one-fifth of the latter (21% at the eighth cycle). This further highlights the key role of composite morphology in its electrochemistry and in the solid electrolyte *in situ* activation.

Given the variety of electrochemical processes occurring within this system, we suggest here a complete and detailed representation (Figure 6) that elucidates the principal contributions to capacity as functions of voltage. Figure 6 illustrates the three main redox pathways that contribute to the accessible capacity: sulfur, iron, and phosphorus. The sulfur redox involves contributions from both FeS2 (red frames) and LPSCl_{1.5} (blue frames), the iron contribution comes exclusively from the CAM, and the phosphorus solely from the SE. These three electrochemical pathways occur in distinct, overlapping redox intervals within the voltage range for ASSLSBs, as displayed in Figure 5d. Besides, they are interconnected, since sulfur plays a role in both iron and phosphorus redox paths. Hence, depending on the voltage range, these systems could be referred to as Li-S-Fe ASSBs, when including also FeS₂.

2.4. Positive Electrode Evolution During Cycling. After the impact of the positive electrode microstructure and its components on the electrochemical performances was assessed, the morphological and chemical evolution of the composite was evaluated. All composites were investigated in the pristine state, after the first discharge and after the first charge. As shown in Figure 7a and in Supporting Information Figure S15, the morphological evolution of the CAM depends on its size. The composite porosity was calculated using SEM

images (Supporting Information Figures S16 and S17). The pore volume fraction decreased after the first lithiation, likely as an adaptation to the local volume increase but did not vanish. The pore volume decreases then again after the first charge, possibly due to the volume contraction of the CAM in the positive electrode and volumetric expansion of the negative electrode. This supports the assumption that the presence of pores can help alleviating reaction-induced volume changes in conversion-type electrodes—to a limited extent. 11 We analyzed the SEM images of the cross sections of the positive electrode composites and different states of charge. From our observations, we hypothesize that in the discharged state small particles (ca. < 100 nm) were uniformly lithiated while medium-sized particles (ca. 100-1000 nm) showed a coreshell structure (Figure 7a). In the shell, radially distributed cracks were present because of the local volume changes. Based on the SEM images we collected, we suggest that large particles (ca. > 1 μ m) were unevenly lithiated, possibly due to local mechanical stresses causing the fragmentation. The so formed fragments seem to follow the lithiation trends, either homogeneous or core-shell structured, previously described for smaller particles. In our SEM observations of the lithiated state, we noted that the CAM displayed similar patterns as observed in the discharged state. Thus, FeS₂ (de)lithiation displacement reaction does not have a preferred direction and rather forms submicro-domains, unlike other conversion materials (e.g., CuS). We attribute this behavior to the much lower mobility of iron ions compared to copper ions in their respective sulfides. 47,48 Elemental mapping of the pristine state (Figure 7) reveals the interconnected pristine microstructure of the positive electrode. In the discharged state, small CAM particles did not show any pattern in sulfur and iron distributions. The core of medium-sized particles was rich in iron and was surrounded by an iron-depleted circle, where the shell had both elements and similar considerations were valid

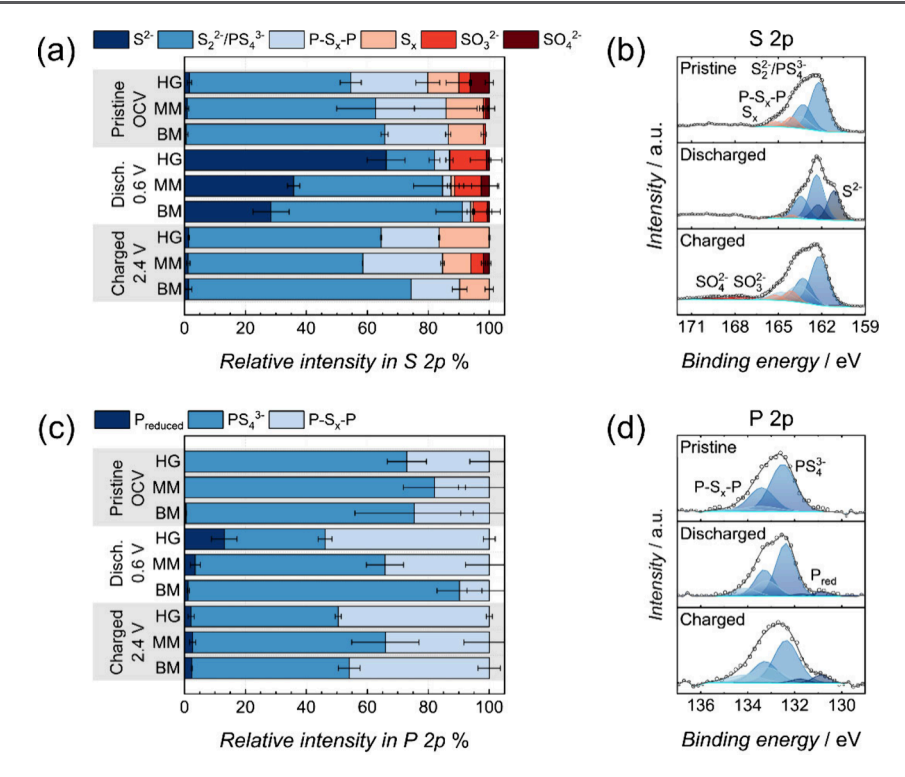


Figure 8. XPS analyses of the $FeS_2/LPSCl_{1.5}/carbon$ black positive electrode composite in the pristine, discharged, and charged states. The composites were prepared with hand grinding (HG), mini mill (MM), and ball mill (BM). Relative intensities in (a) the S 2p and (c) the P 2p detail spectra. Detailed spectra and component assignments of the mini milled positive electrode composites at different states of charge for (b) S 2p and (d) P 2p regions.

in the charged state. The species were thus spatially differently distributed at different states of charge.

To elucidate the evolution of the chemical composition of the FeS₂/LPSCl₁₅/CB positive electrode at different states of charge, ex situ XPS was performed. To assess the data quality, the elements were quantified to ensure that they matched the theoretical amounts (Supporting Information Note S3 and Figure S18). The C 1s spectra show new signals rising in the discharged state which were not found in the following charge. This may be explained by the formation of lithiated carbon species at low potential, which are consumed during subsequent charging (Supporting Information Figure S19). The lithiated components, present on the surface of the carbon black particles, were assigned to both stoichiometric and nonstoichiometric species due to the carbon morphology. This is supported by the partial overlap of the applied voltage range $(1.2-3.0 \text{ V vs. Li}^+/\text{Li})$ with the one of carbon lithiation (0.0-2.5 V vs. Li⁺/Li). 47,49 Therefore, the spectra of samples at the discharged state were calibrated to the binding energy of Cl 2p, which remained constant during cycling due to similar binding energies of LPSCl_{1.5} and LiCl, formed after the initial discharge. The spectra of samples at charged state were calibrated to C 1s. Further information and detailed descriptions and fittings can be found in Supporting Information Note S4 and Figure S19. Sulfur and phosphorus components were evaluated (Figure 8) and their analyses were always in agreement. Specific details on the constraints used for the analysis are reported in Supporting Information Tables T1-T6. In the positive electrodes at the pristine state, FeS₂ (S_2^{2-}) and LPSCl_{1.5} (PS_4^{3-}) were dominant in the S 2p and in the P 2p spectra. The S 2p spectra contained components from FeS₂ and LPSCl_{1.5}, which unfortunately could not be unequivocally distinguished. After the first discharge, the

formation of reduced species (S2- and Preduced, the latter indicating reduced phosphorus in general, not specifically elemental P) at the expense of oxidized components was observed. We ascribe the S²⁻ peak at ca. 160.6 eV to Li₂S, which may form from FeS2 and solid electrolyte with in situ decomposition, or to Li_{2x}FeS. At the same time, the P_{reduced} shoulder (ca. 130.8 eV) in the P 2p spectrum indicates the presence of reduced phosphorus containing species after discharge. These products prove the redox activity of these species and the positive electrode lithiation. After the first charge, the reduced components were oxidized due to delithiation, showing their redox-active nature. A growth of the fractions of S_x (ca. 164.2 eV) and $P-S_x-P$ (ca. 163.3 eV) components was detected in the S 2p spectrum. These are attributed to sulfur chains or rings of unknown lengths and to thiophosphate species, respectively. The latter were identified to be $(Li_2S)_{075}(P_2S_5)_{025}$, $(Li_2S)_{067}(P_2S_5)_{033}$ (i.e., $P_2S_7^{4-}$), and $(\text{Li}_2\text{S})_{050}(\text{P}_2\text{S}_5)_{050}$ (*i.e.*, $\text{P}_2\text{S}_6^{2-}$), and they were also detected in P 2p spectra, validating the assignment. However, due to the variety of sulfur structural units, the detailed pathway is still undefined as well as the origin of the forming species from either the active material or the solid electrolyte.

To summarize, this work discloses the morphology evolution of the electrochemically active species in $\mathrm{FeS_2}$ -based Li -S solid-state cells at different states of charge. The microstructure evolution is dependent on the CAM particle size. Only small particles were homogeneously lithiated, while larger ones presented core—shell structures and cracks. The positive electrode microstructure was proven to greatly impact the accessible capacity and its retention. The formation of lithiated reduced species (e.g., $\mathrm{Li_2S}$ and reduced phosphorus species) at the first discharge and delithiated (i.e., sulfur chains or rings of unknown lengths and to thiophosphate species) products after

the first charge was proven. The changes in the sulfur and phosphorus XPS spectra unequivocally showed the relevant contribution of the solid electrolyte decomposition in ASSLSBs containing transition metal sulfides. The redox path of iron, previously investigated by Wu *et al.*, is supported by this study.³⁷ Furthermore, we show here the redox activity of carbon in Li–S cells at the first discharge.

3. CONCLUSIONS

This study investigated the impact of the positive electrode microstructure on FeS_2 -based ASSLSBs. Finely submicrostructured composites enhanced the electrochemical performance, due to the intimate contact among the components. The SE decomposition led to *in situ* formation of active material which significantly contributed to the overall capacity. To conclude, we observed that the morphological evolution of FeS_2 during cycling depends on the particle size, which makes processing of the positive electrode highly relevant.

Three different mechanical processing methods (*i.e.*, hand grinding, mini mill, and ball mill) were employed to prepare the positive electrodes. Ball milling emerged as the most effective, producing a composite with a uniform and finely divided structure, consisting of submicro-sized FeS₂ and CB domains homogeneously embedded in an SE matrix. This uniformity aided the distribution of mechanical stress and reduced lithium-ion diffusion paths, resulting in higher specific capacity and cycle stability. However, while ball milling improved the overall electrochemical performance, it also caused a reduction in the crystallinity of the solid electrolyte, thereby decreasing its ionic conductivity. The submicrostructured composites, characterized by a large SE/CB contact area, showed a severe contribution of a secondary reversible process: the SE *in situ* decomposition into active material.

The evolution of the electrochemically formed active species from FeS₂ was mapped with SEM-EDS and chemically analyzed with XPS. The microstructure and composition/stoichiometry of FeS₂ evolved during cycling, leading to coreshell structured particles in both the discharged and charged states. Besides, the composite's porosity decreased after the initial discharge, partially relieving the local volume changes. These findings underline the key role of the composite microstructure and the need for fundamental studies to understand its impact on the electrochemical performances.

4. EXPERIMENTAL SECTION

4.1. Materials and Sample Preparations. *4.1.1. Preparation of FeS*₂. Commercially available iron disulfide, powder, 325 mesh, 99.8% trace metals basis (Merck-Sigma-Aldrich GmbH) was used as starting material. The commercial powder was ball milled under Ar atmosphere $(p(O_2)/p < 5 \text{ ppm}, p(H_2O)/p < 5 \text{ ppm})$ with a Fritsch Pulverisette 7 premium line mill (ZrO₂ milling set, 80 mL cups, 5 mm diameter milling media) to reduce its size. Milling was conducted for 12 milling cycles, each of 10 min at 500 rpm followed by a 10 min break.

4.1.2. Preparation of $Li_{5.5}PS_{4.5}Cl_{1.5}$. $Li_{5.5}PS_{4.5}Cl_{1.5}$ was prepared by a high-temperature solid-state synthesis. First, the reactants Li_2S (Thermo Scientific Chemicals, 99.9%), P_2S_5 (Sigma-Aldrich, 99%), and LiCl (Sigma-Aldrich, 99%) were weighed stoichiometrically and mixed in an agate mortar for approximately 15 min. Second, the reactant mixture was densified to pellets using a hand press and placed in quartz ampules. The ampules were previously carbon coated and dried at 800 °C for 1 h under dynamic vacuum. The ampule was then sealed under vacuum, and the reaction was performed at 450 °C for 3 days. Afterward, the synthesis step was repeated, *i.e.*, the synthesis product is mortared, placed in a quartz ampule, heated again to 450

°C, and held for 3 days. The synthesis preparation was performed under Ar atmosphere.

4.1.3. Preparation of All-Solid-State Positive Electrode Composites. Positive electrode composites for all-solid-state Li-S cells were prepared by using the milled FeS2 powder, Li5.5PS4.5Cl1.5, and commercially available Super P conductive carbon black (CB) (MSE supplies). Before the components were mixed, FeS₂ and carbon black powders were dried for 24 h at 300 $^{\circ}\text{C}$ under a dynamic vacuum in a Büchi oven. The positive electrode composites were prepared by (i) hand grinding, (ii) mini mill, or (iii) ball mill. Hand-ground composites were prepared in an agate mortar with the pestle for 10 min. To prepare mini milled composites, a Fritsch Pulverisette 23 (ZrO₂ milling set, 3 mm diameter milling media) was employed. Mini milling was conducted at 30 Hz for 1 h. To prepare ball milled composites, a Fritsch Pulverisette 7 premium line mill (ZrO₂ milling set, 80 mL cups, 5 mm diameter milling media) was employed. The ball milling was conducted for 24 milling cycles of 10 min at 300 rpm, followed by a 10 min break. Positive electrode composites containing FeS₂ were prepared by mixing CAM:SE:CB in 30:50:20 weight ratio (CAM 30 wt %, SE 50 wt % and CB 20 wt % or CAM 14 vol.%, SE 59 vol.%, and CB 27 vol.%). The carbon and SE were used within the composite to ensure sufficient electronic and ionic contact of FeS₂. Positive electrode composites without FeS2 were prepared by mixing SE:CB in a 50:20 weight ratio (SE 71 wt % and CB 29 wt % or SE 68 wt % and CB 31 wt %). Due to the instability of the argyrodite to ambient atmosphere, all samples were always handled under Ar atmosphere $(p(O_2)/p < 5 \text{ ppm}, p(H_2O)/p < 5 \text{ ppm}).$

4.1.4. Cell Assembly for Long-Term Cycling. All-solid-state Li–S cells were assembled in custom-made PEEK casings with a 10 mm inner diameter. An In/InLi alloy was employed as negative electrode, and 80 mg of SE was used as separator. Either 10 mg (for positive electrodes containing FeS₂) or 7 mg (for positive electrodes without FeS₂) of composites were inserted into the PEEK casing. These corresponded to an LPSCl_{1.5} loading of 5 mg (6.4 mg·cm⁻²) and, when present, an FeS₂ loading of 3 mg (3.8 mg·cm⁻²). For densification, the layers were compressed uniaxially for 3 min at 3 tons. The negative electrode was prepared by stacking an indium foil (9 mm diameter, chemPur, 99.995%) and lithium foil (6 mm diameter, Sigma-Aldrich, 99.9%) on the separator. Two polished stainless-steel rods were employed as current collectors. The cells were fixed in a frame, and a pressure of approximately 60 MPa was applied to guarantee mechanical contact during cycling.

4.1.5. Cell Assembly for Partial Conductivity Measurements. All cells for electronic partial conductivities were assembled in custom-made PEEK casings with a 6 mm inner diameter. For measurements, ca. 100 mg of positive electrode composite was loaded. All cells for ionic partial conductivities were assembled in custom-made PEEK casings with a 10 mm inner diameter. For measurements, ca. 50 mg of positive electrode composite was loaded between layers of solid electrolyte (80 mg each). On both sides In/InLi alloy was used and prepared as previously described. For all measurements, two polished stainless-steel rods were employed as current collectors. For densification, the layers were compressed uniaxially for 3 min at 1.1 tons (for 6 mm diameter cells) or 3 tons (for 10 mm diameter cells). The cells were fixed in a frame, and a pressure of approximately 60 MPa was applied to guarantee mechanical contact during electrochemical testing.

4.1.6. Sample Preparation for Ex Situ Analyses. After cycling, the potential was held for 24 h, or until the current dropped below 0.015 mA. The samples were then stabilized at their OCV. The cells were then carefully removed from the cell casing in an Ar-filled glovebox with a hand press. The cross sections were prepared with a Leica EM TIC 3X instrument (Leica Mikrosysteme GmbH). These were cut under vacuum (10^{-6} mbar) for 6 h using three ion guns (6.0 kV and 2.2 mA) and in cryo conditions, liquid nitrogen was used to cool them at $-100\,^{\circ}$ C. The samples were always transferred with a Leica VCT500 airtight transfer module. Directly after cutting, SEM and EDS analyses were performed on the cross sections.

4.2. Characterization. 4.2.1. Electrochemical Testing. Battery cycling was performed at 25 °C with a VMP300 or a VMP-3

potentiostat (Biologic). All cells for long-term cycling were tested under galvanostatic conditions between 0.6 and 2.4 V vs. In/InLi. A four-electron reaction of FeS₂ was assumed for calculating the C-rates, so the theoretical capacity of FeS₂ (894 mAh·g⁻¹) was used. For the characterized model cells, a rate of 0.1 C (341 μ A·cm⁻²) was used. All cells used for the evaluation of long-term cycling performances were built as duplicates or triplicates to ensure reproducibility.

Partial electronic conductivity measurements were performed by impedance and chronoamperometry. The latter method was employed also for partial ionic conductivity. The impedance was measured with an amplitude of 10 mV and in a frequency range of 7 MHz–100 mHz. The impedance spectra were fitted by using the RelaxIS 3 software package (rhd Instruments, Darmstadt, Germany). All the cells were built as duplicates or triplicates to ensure reproducibility.

4.2.2. Dynamic Light Scattering (DLS). DLS measurements were performed with a Nano ZS Zetasizer system (Malvern Instruments, Malvern, UK) at 25 °C. All the measurements were performed three times, and the results were averaged to obtain the final results. A transparent plastic cuvette with a light path of 10 mm and a volume of 3.5 mL was employed. The data were exported by using the corresponding Zetasizer Software.

4.2.3. Particle Size Analysis (PSA). PSA measurements were performed with a HELOS/BR (Sympatec GmbH) instrument with laser diffraction at 25 °C. The measurements were performed in dispersion. The dispersing media for carbon black and FeS₂ was ethanol, for Cl-rich argyrodite a mixture xylene-Oppanol (1 wt %) was employed. All measurements were performed three times, and the results were averaged. A quartz cuvette with a volume of 6 mL was employed. The data was exported using the PAQXOS software.

4.2.4. X-ray Diffraction (XRD). XRD analysis was performed in Bragg—Brentano geometry on a reflection-transmission spinner. The samples were analyzed with an Empyrean 3 diffractometer (Malvern PANalytical) with a Mo K α source (60 kV, 40 mA). The 2 Θ range was 5° to 45° and with a step size of 0.014°.

4.2.5. Scanning Electron Microscopy (SEM). SEM analysis was performed using a Carl Zeiss Merlin electron microscope with an acceleration voltage of 3 kV and aperture size of 20.0 μ m in vacuum (10⁻⁶ mbar). The software used was SmartSEM. The working distance was 2.5–4.0 mm. The procedure to calculate the pore area was adapted from Fujita et al. The pore volume was calculated with GIMP software (version 2.10.38). The pore area fraction was determined by considering the area occupied by the pores with respect to the total rectangular area of the composite in the image. The area of the composite was determined as the total rectangular area minus the area occupied by the pores. For each sample, a region large enough to be representative of the entire sample was analyzed to ensure reliability.

4.2.6. Energy Dispersive X-ray Spectroscopy (EDS). EDS analysis was performed within SEM using an X-Max 50 Silicon Drift Detector (Oxford Instruments) with a polymer window. An acceleration voltage of 10 kV and an aperture size of 60.0 μ m were used at a working distance of 8.5 mm. The software used for the elemental analyses was AZtec 6. The cross sections of the samples post mortem were analyzed first with SEM and then with EDS.

4.2.7. X-ray Photoelectron Spectroscopy (XPS). XPS measurements were conducted by using a PHI VersaProbe IV system (Physical Electronics Inc.). A monochromated Al K_{α} X-ray source (X-ray source 50 W 15 kV with beam diameter of 200 μ m) was used. A step time of 20 ms, a step size of 0.2 eV, and an analyzer pass energy of 55.00 eV were used for the detailed spectra. During measurements, the sample surface was charge-neutralized and the pressure ranged from 10^{-7} to 10^{-6} Pa. The samples were prepared in a glovebox (M. Braun Inertgas-Systeme GmbH, $(O_2 < 5 \text{ ppm}, H_2O < 5 \text{ ppm})$ and transferred from the glovebox to the analysis chamber with a transfer shuttle. The samples were mounted on a sample holder using insulating tape and with the exposed positive electrode surface facing the X-ray beam. The samples were sputtered with a gas cluster ion beam gun (GCIB) (10 Kv 30 nA, $2 \times 2 \text{ mm}^2$, 5 min) to clean the surfaces. Data analysis was performed by using CasaXPS software.

The charge correction was done using C 1s (284.8 eV) if possible, and Cl $2p_{3/2}$ (199.1 eV) otherwise.

ASSOCIATED CONTENT

Solution Supporting Information

The Supporting Information is available free of charge at https://pubs.acs.org/doi/10.1021/acs.chemmater.4c03315.

Characterization of FeS₂ obtained after particle size reduction performed with ball mill: SEM images (Figure S1), particle size distributions (Figure S2), and XRD (Figure S3); characterization of the pristine components used for preparing the positive electrodes: SEM images (Figure S4) and particle size distributions (Figure S5); characterization and electrochemical data of positive electrode composites with FeS₂: XRD (Figure S6), longterm cycling (Figure S7) galvanostatic charge—discharge profiles and differential capacity curves (Figure S8), and Coulomb and conversion efficiencies (Figure S9); partial electronic and ionic conductivity values (Figure S10), DC measurements in electron (Figure S11) and ion blocking (Figure S12) conditions, impedance of the In/ InLilSEIIn/InLi cell (Figure S13), and partial conductivity measurements description (Note S1); characterization and electrochemical data of positive electrode composites without FeS2: XRD (Figure S14) and calculation of FeS₂ and LPSCl_{1.5} contributions (Note S2); ex situ SEM analysis of the positive electrode composites with FeS2 (Figure S15) and observed pore volume areas (Figures S16 and S17); and ex situ XPS analysis of the positive electrode composites with FeS₂: elemental quantification (Note S3 and Figure S18), data calibration and analysis of C 1s and Cl 2p spectra (Note S4 and Figure S19), and tables with fitting parameters and constraints (Tables T1-T6) (PDF)

AUTHOR INFORMATION

Corresponding Author

Jürgen Janek – Institute for Physical Chemistry and Center for Materials Research (ZfM), Justus Liebig University Giessen, Giessen 35392, Germany; ⊚ orcid.org/0000-0002-9221-4756; Email: juergen.janek@pc.jlug.de

Authors

Matilde Pavan – Institute for Physical Chemistry and Center for Materials Research (ZfM), Justus Liebig University Giessen, Giessen 35392, Germany

Konrad Münch — Institute for Physical Chemistry and Center for Materials Research (ZfM), Justus Liebig University Giessen, Giessen 35392, Germany; orcid.org/0000-0002-8778-9344

Sebastian L. Benz – Institute for Physical Chemistry and Center for Materials Research (ZfM), Justus Liebig University Giessen, Giessen 35392, Germany; orcid.org/0000-0002-0650-984X

Tim Bernges — Institute for Inorganic and Analytical Chemistry, University of Münster, Münster 48149, Germany Anja Henss — Center for Materials Research (ZfM) and Institute of Experimental Physics, Justus Liebig University Giessen, Giessen 35392, Germany

Wolfgang G. Zeier — Institute for Inorganic and Analytical Chemistry, University of Münster, Münster 48149, Germany; Institute of Energy Materials and Devices (IMD), IMD-4: Helmholtz-Institut Münster, Forschungszentrum Jülich,

48149 Münster, Germany; o orcid.org/0000-0001-7749-5089

Complete contact information is available at: https://pubs.acs.org/10.1021/acs.chemmater.4c03315

Author Contributions

M.P. developed and performed the experiments, conceptualization, formal analysis, visualization, writing original draft, and editing. K.M. performed design of experiments, investigation, and validation. M.P. and S.L.B. performed XPS investigation and validation. T.B. designed the experiments for the synthesis of the solid electrolyte. W.G.Z. performed review and editing. A.H. performed supervision, visualization, review, and editing. J.J. performed conceptualization, funding acquisition, supervision, visualization, review, and editing. All authors discussed the results and commented on the work.

Notes

The authors declare no competing financial interest.

ACKNOWLEDGMENTS

M.P. and T.B. received support from the Federal Ministry of Education and Research (BMBF) for the project KAROFEST (grant number 03XP0498A). K.M. and S.B. received support within the BMBF projects SoLiS (grant number 03XP0395D) and ProRec (grant number 03XP0537E), respectively. The authors thank Bjoern Luerßen for his help in preparing the Table of Contents graphic. The authors thank Marta Rando for her help in building cells for partial conductivity measurements.

REFERENCES

- (1) Janek, J.; Zeier, W. G. A solid future for battery development. *Nature Energy* **2016**, *1* (9), 16141.
- (2) Minnmann, P.; Strauss, F.; Bielefeld, A.; Ruess, R.; Adelhelm, P.; Burkhardt, S.; Dreyer, S. L.; Trevisanello, E.; Ehrenberg, H.; Brezesinski, T.; Richter, F. H.; Janek, J. Designing Cathodes and Cathode Active Materials for Solid-State Batteries. *Adv. Energy Mater.* 2022, 12 (35), No. 2201425.
- (3) Nitta, N.; Wu, F.; Lee, J. T.; Yushin, G. Li-ion battery materials: present and future. *Mater. Today* **2015**, *18* (5), 252–264.
- (4) Zak, J. J.; Kim, S. S.; Laskowski, F. A. L.; See, K. A. An Exploration of Sulfur Redox in Lithium Battery Cathodes. *J. Am. Chem. Soc.* **2022**, 144 (23), 10119–10132.
- (5) Berger, A.; Freiberg, A. T. S.; Siebel, A.; Thomas, R.; Patel, M. U. M.; Tromp, M.; Gasteiger, H. A.; Gorlin, Y. The Importance of Chemical Reactions in the Charging Process of Lithium-Sulfur Batteries. *J. Electrochem. Soc.* **2018**, *165* (7), A1288–A1296.
- (6) Ye, H.; Sun, J.; Zhang, S.; Lin, H.; Zhang, T.; Yao, Q.; Lee, J. Y. Stepwise Electrocatalysis as a Strategy against Polysulfide Shuttling in Li-S Batteries. *ACS Nano* **2019**, *13* (12), 14208–14216.
- (7) Zhong, Y.; Wang, Q.; Bak, S.-M.; Hwang, S.; Du, Y.; Wang, H. Identification and Catalysis of the Potential-Limiting Step in Lithium-Sulfur Batteries. *J. Am. Chem. Soc.* **2023**, *145* (13), 7390–7396.
- (8) Fittipaldi, F.; Pauciulo, L. Electrical Conductivity Measurements for Good Insulators. *J. Appl. Phys.* **1966**, *37* (11), 4292–4293.
- (9) Fujita, Y.; Münch, K.; Asakura, T.; Motohashi, K.; Sakuda, A.; Janek, J.; Hayashi, A. Dynamic Volume Change of Li₂S-Based Active Material and the Influence of Stacking Pressure on Capacity in All-Solid-State Batteries. *Chem. Mater.* **2024**, *36* (15), 7533–7540.
- (10) Whang, G.; Ketter, L.; Zhao, T.; Nazmutdinova, E.; Kraft, M. A.; Zeier, W. G. High Areal Capacity Cation and Anionic Redox Solid-State Batteries Enabled by Transition Metal Sulfide Conversion. ACS Appl. Mater. Interfaces 2024, 16 (32), 42189–42197.

- (11) Whang, G.; Zeier, W. G. Transition Metal Sulfide Conversion: A Promising Approach to Solid-State Batteries. *ACS Energy Letters* **2023**, 8 (12), 5264–5274.
- (12) Yersak, T. A.; Stoldt, C.; Lee, S.-H. Electrochemical Evolution of an Iron Sulfide and Sulfur Based Cathode for All-Solid-State Li-Ion Batteries. *J. Electrochem. Soc.* **2013**, *160* (8), A1009–A1015.
- (13) Liu, Z.; Li, X.; Zhang, H.; Huang, K.; Yu, Y. Are solid-state batteries absolutely more environmentally friendly compared to traditional batteries-analyzing from the footprint family viewpoint. *Journal of Cleaner Production* **2024**, *447*, No. 141452.
- (14) Liu, Z.; Liao, X.; Zhang, Y.; Li, S.; Ye, M.; Gan, Q.; Fang, X.; Mo, Z.; Huang, Y.; Liang, Z.; Dai, W.; Sun, S. A highly efficient process to enhance the bioleaching of spent lithium-ion batteries by bifunctional pyrite combined with elemental sulfur. *Journal of environmental management* **2024**, 351, No. 119954.
- (15) Whang, G.; Ashby, D. S.; Lapp, A. S.; Hsieh, Y.-C.; Butts, D. M.; Kolesnichenko, I. V.; Wu, P.-W.; Lambert, T. N.; Talin, A. A.; Dunn, B. S. Temperature-Dependent Reaction Pathways in FeS₂: Reversibility and the Electrochemical Formation of Fe₃S₄. *Chem. Mater.* **2022**, 34 (12), 5422–5432.
- (16) de Biasi, L.; Kondrakov, A. O.; Geßwein, H.; Brezesinski, T.; Hartmann, P.; Janek, J. Between Scylla and Charybdis: Balancing Among Structural Stability and Energy Density of Layered NCM Cathode Materials for Advanced Lithium-Ion Batteries. *J. Phys. Chem.* C 2017, 121 (47), 26163–26171.
- (17) Li, L.; Luo, C.; Zou, J.; Ran, Q.; Chen, P.; Wang, X.; Zhao, Y.; Wang, L.; Zheng, J.; Niu, X. Prelithiated FeS₂ cathode with alleviated volume expansion toward improved cycling performance. *Solid State Ionics* **2021**, *368*, No. 115696.
- (18) Butala, M. M.; Mayo, M.; Doan-Nguyen, V. V. T.; Lumley, M. A.; Göbel, C.; Wiaderek, K. M.; Borkiewicz, O. J.; Chapman, K. W.; Chupas, P. J.; Balasubramanian, M.; Laurita, G.; Britto, S.; Morris, A. J.; Grey, C. P.; Seshadri, R. Local Structure Evolution and Modes of Charge Storage in Secondary Li–FeS 2 Cells. *Chem. Mater.* **2017**, 29 (7), 3070–3082.
- (19) Ashby, D. S.; Horner, J. S.; Whang, G.; Lapp, A. S.; Roberts, S. A.; Dunn, B.; Kolesnichenko, I. V.; Lambert, T. N.; Talin, A. A. Understanding the Electrochemical Performance of FeS₂ Conversion Cathodes. ACS Appl. Mater. Interfaces 2022, 14 (23), 26604–26611.
- (20) Walker, B. A.; Plaza-Rivera, C. O.; Sun, S.; Lu, W.; Connell, J. W.; Lin, Y. Dry-Pressed Lithium Nickel Cobalt Manganese Oxide (NCM) Cathodes Enabled by Holey Graphene Host. *Electrochim. Acta* 2020, 362, No. 137129.
- (21) Zou, J.; Zhao, J.; Wang, B.; Chen, S.; Chen, P.; Ran, Q.; Li, L.; Wang, X.; Yao, J.; Li, H.; Huang, J.; Niu, X.; Wang, L. Unraveling the Reaction Mechanism of FeS₂ as a Li-Ion Battery Cathode. *ACS Appl. Mater. Interfaces* **2020**, *12* (40), 44850–44857.
- (22) Schieck, R.; Hartmann, A.; Fiechter, S.; Konenkamp, R.; Wetzel, H. Electrical properties of natural and synthetic pyrite (FeS₂) crystals. *J. Mater. Res.* **1990**, *S* (7), 1567–1572.
- (23) Zeng, X.; Xiao, Y.; Ji, X.; Wang, G. Mineral Identification Based on Deep Learning That Combines Image and Mohs Hardness. *Minerals* **2021**, *11* (5), 506.
- (24) Janek, J.; Zeier, W. G. Challenges in speeding up solid-state battery development. *Nature Energy* **2023**, *8*, 230–240.
- (25) Machín, A.; Cotto, M.; Díaz, F.; Ducongé, J.; Morant, C.; Márquez, F. Environmental Aspects and Recycling of Solid-State Batteries: A Comprehensive Review. *Batteries* **2024**, *10* (7), 255.
- (26) Gil-González, E.; Ye, L.; Wang, Y.; Shadike, Z.; Xu, Z.; Hu, E.; Li, X. Synergistic effects of chlorine substitution in sulfide electrolyte solid state batteries. *Energy Storage Materials* **2022**, *45*, 484–493.
- (27) Wang, S.; Tang, M.; Zhang, Q.; Li, B.; Ohno, S.; Walther, F.; Pan, R.; Xu, X.; Xin, C.; Zhang, W.; Li, L.; Shen, Y.; Richter, F. H.; Janek, J.; Nan, C.-W. Lithium Argyrodite as Solid Electrolyte and Cathode Precursor for Solid-State Batteries with Long Cycle Life. *Adv. Energy Mater.* **2021**, *11* (31), No. 2101370.
- (28) Dewald, G. F.; Ohno, S.; Kraft, M. A.; Koerver, R.; Till, P.; Vargas-Barbosa, N. M.; Janek, J.; Zeier, W. G. Experimental Assessment of the Practical Oxidative Stability of Lithium

- Thiophosphate Solid Electrolytes. Chem. Mater. 2019, 31 (20), 8328-8337.
- (29) Qian, X.; Lyu, Y.; Zhou, S.; Qiu, Y.; Sun, Y.; Yuan, Y.; Shao, M. Enhancing Long Stability of Solid-State Batteries Through High-Energy Ball Milling-Induced Decomposition of Sulfide-Based Electrolyte to Sulfur. *Advanced materials* **2024**, *36*, No. e2412319.
- (30) Keshavarzmohammadian, A.; Cook, S. M.; Milford, J. B. Cradle-to-gate environmental impacts of sulfur-based solid-state lithium batteries for electric vehicle applications. *Journal of Cleaner Production* **2018**, 202, 770–778.
- (31) Bai, X.; Jiang, Di; Yin, S.; Hao, Y.; Zheng, J.; Hao, H.; Xing, J.; Dong, J.; Liu, H.; Liao, L. Pyrite-Based Solid-State Batteries: Progresses, Challenges, and Perspectives. *Adv. Funct. Mater.* **2025**, 35, 2416808.
- (32) Ulissi, U.; Ito, S.; Hosseini, S. M.; Varzi, A.; Aihara, Y.; Passerini, S. High Capacity All-Solid-State Lithium Batteries Enabled by Pyrite-Sulfur Composites. *Adv. Energy Mater.* **2018**, *8* (26), No. 1801462.
- (33) Douglas, A.; Carter, R.; Oakes, L.; Share, K.; Cohn, A. P.; Pint, C. L. Ultrafine Iron Pyrite (FeS₂) Nanocrystals Improve Sodium-Sulfur and Lithium-Sulfur Conversion Reactions for Efficient Batteries. ACS Nano 2015, 9 (11), 11156–11165.
- (34) Kaur, H.; Tian, R.; Roy, A.; McCrystall, M.; Horvath, D. V.; Lozano Onrubia, G.; Smith, R.; Ruether, M.; Griffin, A.; Backes, C.; Nicolosi, V.; Coleman, J. N. Production of Quasi-2D Platelets of Nonlayered Iron Pyrite (FeS₂) by Liquid-Phase Exfoliation for High Performance Battery Electrodes. ACS Nano 2020, 14 (10), 13418–13432.
- (35) Dewald, G. F.; Liaqat, Z.; Lange, M. A.; Tremel, W.; Zeier, W. G. Influence of Iron Sulfide Nanoparticle Sizes in Solid-State Batteries. *Angew. Chem.* **2021**, *60* (33), 17952–17956.
- (36) Wei, C.; Wang, R.; Wu, Z.; Luo, Q.; Jiang, Z.; Ming, L.; Yang, J.; Wang, L.; Yu, C. Revealing the size effect of FeS₂ on solid-state battery performances at different operating temperatures. *Chin. Chem. Lett.* **2024**, 35, No. 108717.
- (37) Wu, Z.; Zhang, W.; Xia, Y.; Huang, H.; Gan, Y.; He, X.; Xia, X.; Zhang, J. A comprehensive cognition for the capacity fading mechanism of FeS₂ in argyrodite-based all-solid-state lithium battery. *EcoMat* **2023**, *5* (4), No. e12327.
- (38) Yersak, T. A.; Macpherson, H. A.; Kim, S. C.; Le, V.-D.; Kang, C. S.; Son, S.-B.; Kim, Y.-H.; Trevey, J. E.; Oh, K. H.; Stoldt, C.; Lee, S.-H. Solid State Enabled Reversible Four Electron Storage. *Adv. Energy Mater.* **2013**, 3 (1), 120–127.
- (39) Sun, N.; Liu, Q.; Cao, Y.; Lou, S.; Ge, M.; Xiao, X.; Lee, W.-K.; Gao, Y.; Yin, G.; Wang, J.; Sun, X. Anisotropically Electrochemical-Mechanical Evolution in Solid-State Batteries and Interfacial Tailored Strategy. *Angew. Chem.* **2019**, *58* (51), 18647–18653.
- (40) Minnmann, P.; Quillman, L.; Burkhardt, S.; Richter, F. H.; Janek, J. Editors' Choice—Quantifying the Impact of Charge Transport Bottlenecks in Composite Cathodes of All-Solid-State Batteries. J. Electrochem. Soc. 2021, 168 (4), 040537.
- (41) Liu, W.; Zhao, Y.; Yi, C.; Hu, W.; Xia, J.; Li, Y.; Liu, J. Synergistic Coupling of Sulfide Electrolyte and Integrated 3D FeS₂ Electrode Toward Long-Cycling All-Solid-State Lithium Batteries. *Energy & Environtal Materials* **2024**, *7* (5), No. e12719.
- (42) Zhu, Y.; Fan, X.; Suo, L.; Luo, C.; Gao, T.; Wang, C. Electrospun FeS₂@Carbon Fiber Electrode as a High Energy Density Cathode for Rechargeable Lithium Batteries. *ACS Nano* **2016**, *10* (1), 1529–1538.
- (43) Welch, C.; Cho, K. T.; Srinivasan, V. Modeling Analysis of Ball-Milling Process for Battery-Electrode Synthesis. *Chem. Mater.* **2024**, 36 (14), 6748–6764.
- (44) Maus, O.; Lange, M. A.; Frankenberg, F.; Stainer, F.; Faka, V.; Schlautmann, E.; Rosenbach, C.; Jodlbauer, A.; Schubert, J.; Janek, J.; Li, C.; Michalowski, P.; Wilkening, H. M. R.; Kwade, A.; Zeier, W. G. Influence of Post-Synthesis Processing on the Structure, Transport, and Performance of the Solid Electrolyte Li_{5.5}PS_{4.5}Cl_{1.5} in All-Solid-State Batteries. *Advanced Energy Materials* **2025**, *15* (5), 2403291.

- (45) Dewald, G. F.; Ohno, S.; Hering, J. G. C.; Janek, J.; Zeier, W. G. Analysis of Charge Carrier Transport Toward Optimized Cathode Composites for All-Solid-State Li—S Batteries. *Batteries & Supercaps* **2021**, *4* (1), 183–194.
- (46) Ohno, S.; Koerver, R.; Dewald, G.; Rosenbach, C.; Titscher, P.; Steckermeier, D.; Kwade, A.; Janek, J.; Zeier, W. G. Observation of Chemomechanical Failure and the Influence of Cutoff Potentials in All-Solid-State Li–S Batteries. *Chem. Mater.* **2019**, *31* (8), 2930–2940.
- (47) Santhosha, A. L.; Nazer, N.; Koerver, R.; Randau, S.; Richter, F. H.; Weber, D. A.; Kulisch, J.; Adermann, T.; Janek, J.; Adelhelm, P. Macroscopic Displacement Reaction of Copper Sulfide in Lithium Solid-State Batteries. *Adv. Energy Mater.* **2020**, *10* (41), No. 2002394.
- (48) Zhang, Z.; Dong, K.; Mazzio, K. A.; Hilger, A.; Markötter, H.; Wilde, F.; Heinemann, T.; Manke, I.; Adelhelm, P. Phase Transformation and Microstructural Evolution of CuS Electrodes in Solid-State Batteries Probed by In Situ 3D X-Ray Tomography. *Adv. Energy Mater.* **2023**, *13* (2), 2203143.
- (49) Nam, K.-H.; Hwa Chae, K.; Choi, J.-H.; Jeon, K.-J.; Park, C.-M. Superior carbon black: High-performance anode and conducting additive for rechargeable Li- and Na-ion batteries. *Chemical Engineering Journal* **2021**, *417*, No. 129242.